

Deep Generative Model with Beta Bernoulli Process for Modeling and Learning Confounding Factors

Prashna K Gyawali,¹ Cameron Knight,¹ Sandesh Ghimire,¹ B. Milan Horacek,² John L. Sapp,² Linwei Wang¹

¹ Rochester Institute of Technology, Rochester, USA

² Dalhousie University, Halifax, NS, Canada

fpkg2182@rit.edu

Abstract

While deep representation learning has become increasingly capable of separating task-relevant representations from other confounding factors in the data, two significant challenges remain. First, there is often an unknown and potentially infinite number of confounding factors coinciding in the data. Second, not all of these factors are readily observable. In this paper, we present a deep conditional generative model that learns to disentangle a task-relevant representation from an unknown number of confounding factors that may grow infinitely. This is achieved by marrying the representational power of deep generative models with Bayesian non-parametric factor models, where a supervised deterministic encoder learns task-related representation and a probabilistic encoder with an Indian Buffet Process (IBP) learns the unknown number of unobservable confounding factors. We tested the presented model in two datasets: a handwritten digit dataset (MNIST) augmented with colored digits and a clinical ECG dataset with significant inter-subject variations and augmented with signal artifacts. These diverse data sets highlighted the ability of the presented model to grow with the complexity of the data and identify the absence or presence of unobserved confounding factors.

Introduction

Confounding factors are inherent in most data analyses, especially those of clinical data (Skelly, Dettori, and Brodt 2012). While recent developments in deep representation learning have increased our ability to separate task-relevant representations of the data from other factors of variation (Bengio, Courville, and Vincent 2013), existing works are yet able to address two important challenges. First, in data collected in a realistic setting, there often coincides an unknown and sometimes infinite number of confounding factors. Examples in clinical data include patient demographics (such as sex and age), disease subgroups, data acquisition modalities, and data artifacts and noises. Second, while some confounding factors are easily observable (such as age and sex), others are not. Examples of the latter include unknown data artifacts/noises, or inter-subject variability in physiological factors such as organ anatomy.

Existing deep learning approaches for addressing confounding factors can be broadly divided into the following categories. *Fair representation* learning – commonly used for confounding filtering – encodes data while obfuscating

one or several observed confounding factors (Zemel et al. 2013). Alternatively, *domain adaptation* learns representations invariant to domains where – in the setting of confounding factors – domains can be interpreted as groups with one particular set of variations (Wang and Deng 2018). Both approaches, however, are not applicable when confounding factors are not observed, may exist in large numbers, or may grow infinitely. More generally, *disentangled representation* learning aims to separate all the factors of variations within the data, without explicit assumptions on the number or observability of the confounding factors. However, despite increasing efforts on improving the complexity of the latent structure being modeled by this type of approaches, limited works have explored the modeling and inference of an infinite number of confounding factors.

The Beta Bernoulli process also referred to as an Indian Buffet Process (IBP), is a popular Bayesian nonparametric latent feature model able to represent observations with infinitely many features (Griffiths and Ghahramani 2011). To combine the capacity of IBP to grow with the complexity of the latent structure with the representational capacity of deep networks, recent works have started to explore the use of IBP as a prior in deep generative models like variational auto-encoders (VAE) (Chatzis 2014; Singh, Ling, and Doshi-Velez 2017). These works, however, have not considered the context of disentangling confounding factors. In this paper, we introduce a deep conditional generative model that learns to disentangle a task-relevant representation from an unknown number of confounding factors that may grow infinitely. This is achieved by using a supervised deterministic encoder to learn task-related representation, along with a probabilistic encoder with an IBP prior to model the unknown number of unobservable confounding factors. We term this model as conditional IBP-VAE (cIBP-VAE).

To study the effect of the presented model, we considered two distinct datasets: the MNIST handwritten-digit dataset and a clinical electrocardiogram (ECG) dataset – both augmented with a binary confounding factor in addition to their inherent confounding variations. We focused on the ability of the presented cIBP-VAE model 1) to grow with the complexity of the data as additional confounding factors are introduced, and 2) to identify the absence or presence of binary confounding factors, in comparison to the standard

conditional-VAE (c-VAE) and other baseline models when appropriate. In the MNIST dataset that is inherently confounded by handwriting styles, we introduced a binary confounding factor of color in the digits. In the clinical ECG dataset, we trained the presented model to use the morphology of 12-lead ECG signals to localize the corresponding origin of electrical activation in the heart. This dataset was heavily confounded by a variety of factors, one of the most significant being inter-subject variations in organ anatomy such as the position, orientation, shape, and structural remodeling of the heart (Stevenson 2009). In addition, we augmented this dataset with signal artifacts in the form of a pacing stimulus. Experiment results demonstrated the improved performance of the presented cIBP-VAE in the main task in comparison to a standard c-VAE as the complexity of the data grows, and its ability to – among other unknown confounding factors – identify the absence or presence of binary confounding factors in its latent features.

Related Works

The presented work is closely related to learning *fair* representations (Zemel et al. 2013; Louizos et al. 2015) and its application in confounder filtering (Wu et al. 2018). The notion of learning *fair* representations was introduced in (Zemel et al. 2013) to learn a good representation of the data by obfuscating information related to an observed sensitive attribute such as the age or sex (Zemel et al. 2013). This idea was extended in (Louizos et al. 2015) to leverage the representation power of deep generative models, where Maximum Mean Discrepancy (MMD) was used to learn features invariant to the observed confounding variables. In the application to a health-care domain, an approach was presented in (Wu et al. 2018) to remove the effect of confounding factors by identifying network weights that are associated with confounding factors in the pre-trained model. All of these works considered a small number of observed confounding factors.

The unsupervised modeling of confounding factors is pertinent to the unsupervised learning of disentangled representations (Higgins et al. 2016; Chen et al. 2016a; Kulikarni et al. 2015). Developments of these algorithms are often considered in the context of deep generative models, especially the VAE (Kingma and Welling 2013; Rezende, Mohamed, and Wierstra 2014). While the latent variables are often modeled with an isotropic Gaussian prior in the VAE (Burda, Grosse, and Salakhutdinov 2015), recent works have investigated the use of priors that can model more complex data structures, such as a Gaussian mixture prior (Dilokthanakul et al. 2016) and an autoregressive prior (Chen et al. 2016b). The use of Bayesian nonparametric mixture models as a prior was also considered in (Nalisnick and Smyth 2016; Goyal et al. 2017) to learn an unbounded (infinite) number of clusters in the data in an unsupervised way. By the nature of the mixture model, each data point is assumed to belong to a single class (cluster).

The infinite latent feature models are the Bayesian nonparametric counterpart of latent feature models. Unlike infinite mixture models, they assume that each data point can be produced by multiple classes and represented by multiple latent features, through a binary vector that indicates the pres-

ence or absence of each feature within an infinite number of latent features in the data (Griffiths and Ghahramani 2011). Initial recent works have been presented to use infinite factor models as a prior, especially that realized by the IBP (Griffiths and Ghahramani 2011), within the VAE (Chatzis 2014; Singh, Ling, and Doshi-Velez 2017). These initial works, however, have not considered the context of disentangling or learning confounding factors, nor have in-depth analyses been carried out regarding how an IBP prior may improve the ability of the VAE to grow with the complexity of the data or identify the absence or presence of latent features within the data.

Model

Background: Beta-Bernoulli Process

Beta-Bernoulli Process is a stochastic process which defines a probability distribution over sparse binary matrices indicating the feature activation for K features. The generative Beta-Bernoulli process taking the limit as $K \rightarrow \infty$ is also referred to as the IBP (Griffiths and Ghahramani 2011). The infinite binary sparse matrices is the representation of latent feature allocations $Z \in \{0, 1\}^{N \times K^+}$, where $z_{n,k}$ is 1 if feature k is active for the n^{th} sample and 0 otherwise. For practical implementations, stick-breaking construction (Teh, Grür, and Ghahramani 2007) is considered where the samples are drawn as:

$$z_{n,k} \sim \text{Bernoulli}(\pi_k); \pi_k = \prod_{i=1}^k \nu_i$$

where α and β are the shape parameters for the Beta process. This two-parameter can be relaxed to $(\alpha, 1)$ to recover IBP (Thibaux and Jordan 2007), with α now a hyperparameter representing expected number of features of each data point. For brevity, the whole process is written as $Z, \nu \sim \text{IBP}(\alpha)$.

Conditional generative model

In this work, we introduce a conditional probabilistic model admitting two different sources of variations: the task-related representation y_t , and the confounding representation y_c . Considering factor y_t as an observed variable, the model can be represented as:

$$y_c \sim p(y_c); X \sim p_\theta(X | y_c, y_t)$$

where the latent variable y_c follows a prior distribution $p(y_c)$. To model an unbounded number of unobserved confounders, we model $p(y_c)$ with an IBP prior and arrive at our generative model as:

$$Z, \nu \sim \text{IBP}(\alpha); A_n \sim \text{N}(0, I); y_c = Z \odot A \quad (1)$$

$$X \sim p_\theta(X | Z \odot A, y_t)$$

where \odot is the element-wise matrix multiplication operator, known as the Hadamard product. The multiplication with the discrete-variable Z essentially allows the model to infer which latent features captured by $A_{nk}, k \in 1, \dots, K \rightarrow \infty$ is active for the observed data X . The likelihood function $p_\theta(X | Z \odot A, y_t)$ is defined by neural networks parameterized by θ . The proposed generative model is shown in Figure 1 (a). The corresponding generative model with an isotropic Gaussian prior for y_c is shown in Figure 1 (b).

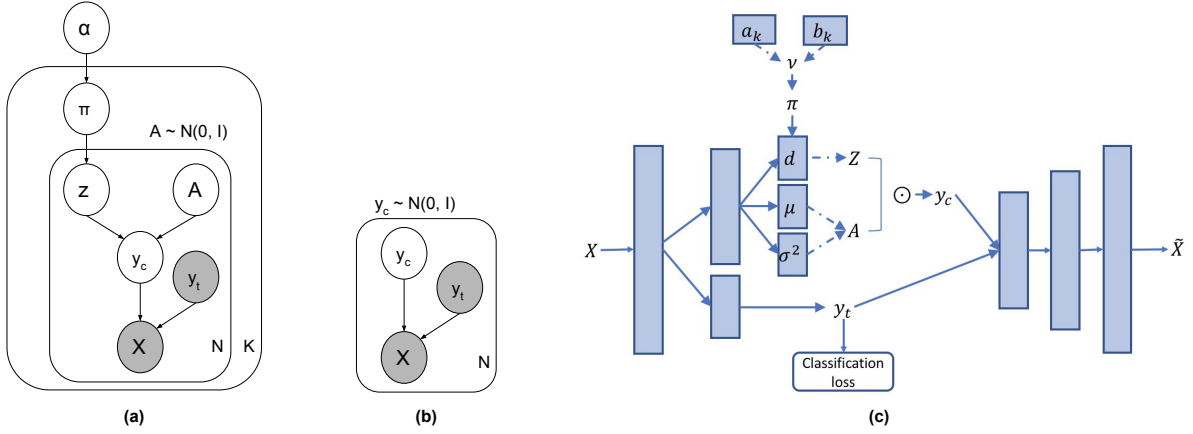


Figure 1: (a) The presented conditional generative model with the confounding representation y_c generated from an IBP prior, in comparison to (b) where y_c is modeled by the standard isotropic Gaussian prior $\mathcal{N}(0, I)$. (c) The overall network architecture for the presented cIBP-VAE.

Inference

To infer latent variables Z, A and ν , we use variational inference where we propose a variational posterior $q_{\phi_1}(Z, A, \nu | X, y_t)$ as an approximation for the true posterior $p(Z, A, \nu | X, y_t)$. To include the dependency between conjugate exponential families within the Beta-Bernoulli process, instead of mean-field approximation that makes strong assumptions regarding the independence of the variables, we adopt the structured stochastic variational inference (SSVI) (Hoffman and Blei 2015). The decomposition of our variational posterior is performed as:

$$q_{\phi_1}(Z, A, \nu | X, y_t) = \prod_{k=1}^K q(\nu_k) \prod_{n=1}^N q(z_{n,k} | \nu_k, x_n) q(A_n | x_n) \quad (2)$$

where $q(\nu_k) = \text{Beta}(\nu_k | a_k, b_k)$, $q(z_{n,k} | \nu_k, x_n) = \text{Bernoulli}(z_{n,k} | \pi_k, d(x_n))$, $\pi_k = \prod_{i=1}^k \nu_i$, $q(A_n | x_n) = \text{N}(A_n | \mu(x_n), \sigma^2(x_n))$, N represents the number of samples, and K represents the truncation parameter as an approximation of infinite feature allocation. Here, ν_k is the global variable shared between data points, and $z_{n,k}$ and A_n are the local variables. a_k and b_k are the parameters, and $d(x_n)$, $\mu(x_n)$ and $\sigma^2(x_n)$ are encoder networks parameterized by ϕ_1 .

Minimizing the Kullback-Leibler (KL) divergence between $q_{\phi_1}(Z, A, \nu | X, y_t)$ and $p(Z, A, \nu | X, y_t)$ can be achieved by maximizing the evidence lower bound (ELBO):

$$\begin{aligned} \log p(X, y_t) \quad \mathcal{L} &= \mathbb{E}_q \left[\log \frac{p(X, y_t, Z, \nu, A)}{q(Z, \nu, A | X, y_t)} \right] \\ &= \sum_{k=1}^K \mathbb{E}_q \left[\log \frac{p(\nu_k)}{q(\nu_k)} + \sum_{n=1}^N \mathbb{E}_q \left[\log \frac{p(x_n, y_{tn}, Z_n | \nu_k)}{q(Z_n | \nu_k, x_n)} \right] \right] \\ &+ \sum_{n=1}^N \mathbb{E}_q \left[\log \frac{p(x_n, y_{tn}, A_n)}{q(A_n | x_n)} \right] \end{aligned}$$

$$\begin{aligned} &= \sum_{k=1}^K \int_{\nu_k} q(\nu_k) \left(\log \frac{p(\nu_k)}{q(\nu_k)} \right. \\ &+ \sum_{n=1}^N \int_{Z_n} q(Z_n | \nu_k, x_n) \log \frac{p(x_n, y_{tn}, Z_n | \nu_k)}{q(Z_n | \nu_k, x_n)} dz_n \Big) d\nu_k \quad (3) \\ &+ \sum_{n=1}^N \int_{A_n} q(A_n | x_n) \log \frac{p(x_n, y_{tn}, A_n)}{q(A_n | x_n)} dA_n \end{aligned}$$

where the second term in equation (3) is itself a lower bound (local ELBO) on the marginal probability of the n th group of observations:

$$\begin{aligned} &\int_{Z_n} q(Z_n | \nu_k, x_n) \log \frac{p(x_n, y_{tn}, Z_n | \nu_k)}{q(Z_n | \nu_k, x_n)} dz_n \\ &= KL(q_{Z_n | \nu_k, x_n} || p_{Z_n | X_n, y_{tn}, \nu_k}) + \log p(x_n, y_{tn} | \nu_k) \\ &\log p(x_n, y_{tn} | \nu_k) \end{aligned} \quad (4)$$

For a given global variable ν_k , we can thus maximize the global ELBO over $q(Z_n | \nu_k, x_n)$ by minimizing the KL divergence between $q(Z_n | \nu_k, x_n)$ and $p(Z_n | X_n, y_{tn}, \nu_k)$. Similar to (Hoffman and Blei 2015), a vector-valued function $\gamma_n(\nu_k)$ is assumed to control the dependency between ν_k and Z_n such that $\gamma_n(\nu_k)$ is at a local maximum of the ‘‘local ELBO’’ and is implicitly achieved within the recognition network (a stochastic encoder).

Once this dependency is specified, the resulting simplified objective is to maximize the following lower bound:

$$\begin{aligned} \mathcal{L} &= KL(q(\nu_k) || p(\nu_k)) + \sum_{n=1}^N \left(\mathbb{E}_q \left[\log p(x_n | Z_n, A_n, y_{tn}) \right] \right. \\ &\quad \left. KL(q(Z_n | \nu, x_n) || p(Z_n | \nu)) \quad KL(q(A_n | x_n) || p(A_n)) \right) \end{aligned} \quad (5)$$

Here, we approximate the expectations by first taking a global sample $\nu_k \sim q(\nu_k)$, and then sample from $Z_n \sim q(Z_n | \nu_k, x_n)$ through the encoder network. This objective

Algorithm 1: cIBP-VAE

input: Dataset X and labels \tilde{y}_t **output:** Optimized model parameters θ^* , ϕ_1^* and ϕ_2^*

- 1 Initialize model parameters θ , ϕ_1 and ϕ_2
 - 2 **for each epoch** $e \in 2E$ **do**
 - for each minibatch** $m \in 2M$ **do**
 - x_m, y_{tm} current minibatch
 - $\nu_k \sim q_{\phi_1}(\nu_k)$ global sample
 - $\pi_k = \prod_{i=1}^k \nu_i$
 - $z_m \sim q_{\phi_1}(z_m | \pi_k, d(x_m))$ local sample
 - $A_m \sim q_{\phi_1}(A_m | \mu(x_m), \sigma(x_m))$
 - $y_c^{(m)} = z_m \cdot A_m$ confounding representation
 - $y_t^{(m)} = q_{\phi_2}(y_t^{(m)} | x_m)$ task-based representation
 - $\tilde{x}_m = p_{\theta}(y_t^{(m)}, y_c^{(m)})$ decoder
 - L^γ Maximize the objective in equation (6) by updating (θ, ϕ_1, ϕ_2)
-

function can be interpreted as minimizing a reconstruction error in the second term, along with minimizing the KL divergence between the variational posterior approximation and the corresponding priors on all the other terms.

Summary of the model

The presented generative model is conditioned on the task-representation y_t that is encoded from data X through a deterministic encoder $f_{y_t}(X)$. Due to the use of a deterministic encoder, however, all sources of stochasticity in y_t are only from the data distribution. To encourage the model to learn discriminative representation in y_t , we extended the unsupervised objective L in equation (5) with a supervised classification loss:

$$L^\gamma = L + \zeta \mathbb{E}_{p(X, y_t)}[\log q_{\phi_2}(y_t | X)] \quad (6)$$

where the hyper-parameter ζ controls the relative weight between the generative and discriminative learning. $q_{\phi_2}(y_t | X)$ is the label predictive distribution (Kingma et al. 2014) approximated by the deterministic encoder $f_{y_t}(X)$ parameterized by ϕ_2 .

Figure 1(c) summarizes the schematic diagram of the overall network architecture of the presented cIBP-VAE model, where the stochastic encoder parameterized by ϕ_1 and the deterministic encoder parameterized by ϕ_2 , respectively, encodes y_c and y_t representation. We synthesize these encoded representations using a decoder network parameterized by θ to generate the reconstructed data \tilde{X} . The overall training procedure of the presented cIBP-VAE is summarized in Algorithm 1.

Experiments

We first augmented the MNIST dataset with colored digits to test the ability of the presented cIBP-VAE – through its latent binary features – to identify the presence or absence

of the factor of color in addition to disentangling the digit from the handwriting style. We then compared the presented cIBP-VAE with c-VAE on a real clinical ECG dataset with significant inter-subject variations and augmented with signal artifacts. This allowed us to test not only the ability of the presented cIBP-VAE to identify the presence or absence of the artifact but also its ability to grow with the complexity of the dataset in comparison to the standard c-VAE.

Implementation details The presented cIBP-VAE requires posterior inferences, involving Bernoulli and Beta random variables, which are not straightforward because they lack the differentiable parameterization that SSVI requires. We thus approximate the Bernoulli random variable Z with the *Concrete distribution* that has a convenient parametrization (Maddison, Mnih, and Teh 2016) (see supplementary material, 1.1). For the Beta distribution, $\text{Beta}(\alpha, \beta)$, we approximate using the Kumaraswamy distribution, $\text{Kumaraswamy}(a_k, b_k)$ as shown by (Nalisnick and Smyth 2016) (see supplementary material, 1.2). Since the two-parameter of $\text{Beta}(\alpha, \beta)$ can be relaxed to $(\alpha, 1)$ to recover IBP, we set the β parameter as 1 in all our experiments.

For all models considered in this work, two hidden layers of 500 units each with ReLU activation are used for both the encoder and decoder. For y_c , each of the involved functions is implemented using a hidden layer with the number of units equal to the truncation number (K) of variational posterior. For y_t , hidden layer of 10 units representing class scores are used. For colored MNIST, we set $K = 100$ and trained the models for $\alpha = 30$. For ECG dataset, we add batch-normalization (Ioffe and Szegedy 2015) after the encoded representations with $\alpha = 20$ and $K = 50$. For optimization, we use Adam (Kingma and Ba 2014) with parameters $\beta_1 = 0.9$, $\beta_2 = 0.999$ and learning rate of $1e-4$ for colored MNIST and $1e-3$ for ECG dataset. For all the datasets, the weight values $\zeta = \{0.5, 0.8, 1.0\}$ are used to find the best model.

For the other models considered for comparison, the same parameters and architecture are used whenever possible. In the clinical ECG dataset, the presented cIBP-VAE was compared to a linear classifier using the commonly-used feature of 120-ms QRS integral (Sapp et al. 2012), as well as a CNN consisting of three-layered convolution blocks (dropout, 2d convolution, batch-normalization, ReLU, and max-pool layer) followed by two fully connected layers. Details about the architectures of these baseline models are included in the supplementary material (sections 2.1 and 2.2). In all experiments, a validation set was used to select the hyper-parameters involved during the training of the model. All the networks were implemented with PyTorch (Paszke et al. 2017).

Colored MNIST

We augment the black-and-white MNIST dataset (LeCun et al. 1998) by adding red, green and blue color to $3/4^{th}$ of the white characters, resulting in 4 types of colors in the dataset with input size of 2352 ($3 \times 28 \times 28$). This adds a binary confounding factor to *style* variations inherent in the original dataset. We focus on the ability of the presented cIBP-VAE

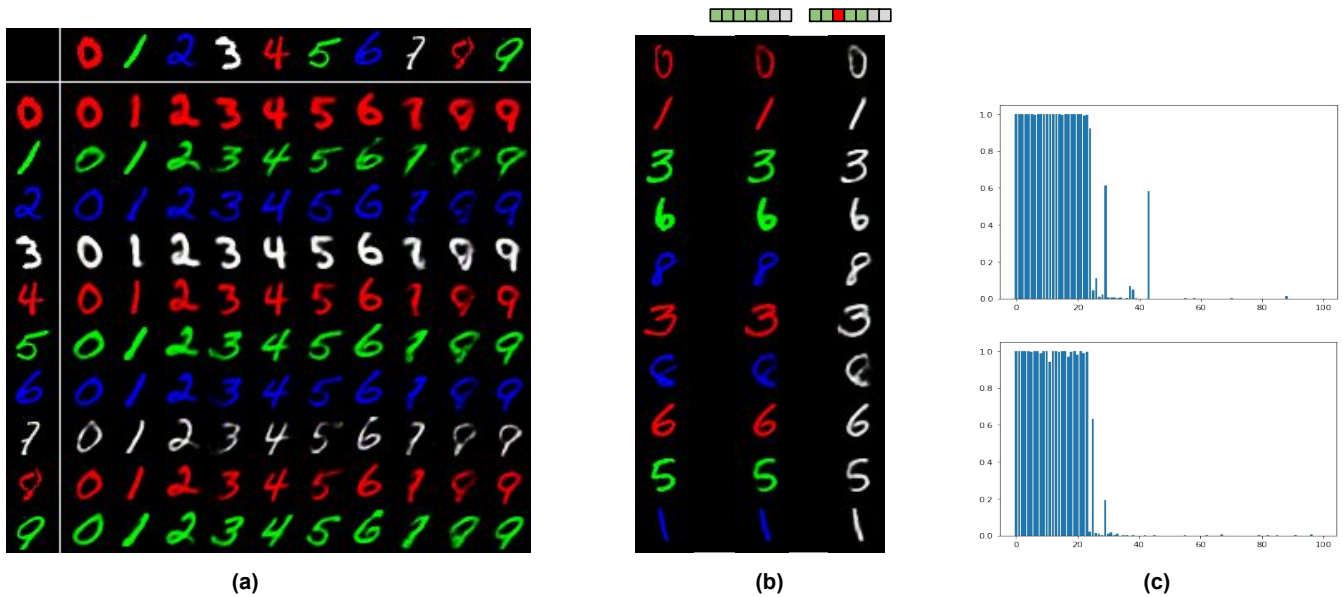


Figure 2: [Best viewed in color] (a) A visualization grid of colored MNIST images by swapping the digit representation from the top-most row with the confounding representation from the left-most column, *i.e.*, hand-writing style and color are transferred from the digits on the leftmost column to each of the ten digits, (b) Examples of original images (left column), reconstructions (middle column), and reconstructions with manually de-activating the triggering units (right column). (c) An example of the bar diagram of the active units in Z , showing a higher number of active features for colored image (top) compared to non-colored image (bottom).

to grow with and identify the absence or presence of this binary confounding factor.

Figure 2 shows examples of swapping y_t (digit representation) and y_c (confounding representation) from a pair of input images using the trained cIBP-VAE. As shown, the confounding representation extracted from one image (left most of each row) – including both the style and color information – can be well transferred to most of the ten digits.

Within the confounding representation y_c , throughout all test cases, we found that colored images were encoded with 26 active binary features, while non-colored images (*i.e.*, white characters) were encoded with 24 active binary features (Figure 2 (c)). This suggests that specific units within the binary features Z were responsible for recognizing the absence or presence of color in these images. We identified these *triggering units* through extensive testing on the trained network, which can be de-activated to remove colors from a given image. Figure 2 (b) provides such examples where the color of a digit was removed by manually turning off the same triggering units in the network.

Clinical ECG dataset

Study cohort: A large pace-mapping ECG dataset is collected from 39 scar-related ventricular arrhythmia patients during invasive pace mapping procedures. Study protocols were approved by the Institutional Research Ethics Board of Dalhousie University. The dataset consists of 15-second 12-lead ECG recordings from 1012 distinctive and recorded pacing points on the left-ventricular (LV) endocardium. Following pre-processing, as described in (Chen et al. 2017),

we obtained a dataset of 16848 unique ECG beats with input size of 1200 (12×100), along with the labeled origins of ventricular activation (pacing sites).

The clinical ECG dataset comprises an infinite number of confounding factors due to inter-subject variations in heart anatomy, thorax anatomy, and pathological remodeling, all unobservable. To test the ability of the presented cIBP-VAE to grow with the complexity of the data, we further augmented this dataset by an artifact (of size 10 for each lead) – in the form of an artificial pacing stimulus – to 50% of all ECG data, selected randomly. For the rest, we augment with all 0’s of the same size, representing no stimulus. The entire dataset was split into training, validation and test set where no set shared data from the same patient.

We focused on two important questions in the experiments. First, how does the presented cIBP-VAE grow with the complexity of the data as additional confounders are introduced, in comparison to the standard c-VAE and other baseline models? Second, whether the latent binary features in the presented cIBP-VAE can identify the presence and absence of the binary confounder of signal artifacts?

Growth with data complexity: To examine how the presented cIBP-VAE grows with the complexity of the data, we considered its performance in 1) classification accuracy and 2) confounder disentanglement before and after the artifacts were introduced to the dataset.

Classification accuracy: For the classification purpose, the pacing sites are transformed into 10 anatomical segments following the setup in (Yokokawa et al. 2012). Table 1 summarizes the localization accuracy of cIBP-VAE in both set-

Model	Seg. classification (in %)	Seg. classification with artifacts (in %)
QRS Int	47.61	-
CNN	53.89	52.44
c-VAE	55.97	53.95
cIBP-VAE	57.53	56.97

Table 1: Segment classification (with and without artifacts) accuracy of the presented method versus three alternative models. Classification accuracy is reported in percentage on the separately held-out test dataset.

factor	anatomical segment		patient ID	
	(w/o)	(w)	(w/o)	(w)
y_t	57.53	56.97	22.06	23.09
y_c	31.24	30.54	66.60	66.48
random-chance	10		4.5	

Table 2: Classification accuracy (in %) when one factor is associated with the label of the other factor. For each classification types, (w) and (w/o) represents with- and without artificial artifacts in the data.

tings, in comparison to the three aforementioned models. Note that we did not include the linear classification model after the pacing artifact is introduced because the extraction of QRS-integrals requires the removal of pacing artifacts. As shown in Table 1, it is evident that, through confounder disentanglement, the two conditional models achieved higher accuracy in both settings. Furthermore, the presented cIBP-VAE outperformed the c-VAE in both settings, demonstrating the benefit of using the IBP as a prior to model complex confounder. Importantly, while all models showed a decrease in classification accuracy when pacing artifacts were introduced to the data, the presented cIBP-VAE exhibited the smallest margin of accuracy loss (# 0.56%) in comparison to the c-VAE (# 2.02%) and CNN (# 1.45%). The reported results are found to be statistically significant (p-value < 0.03) and suggest an improved ability of the presented cIBP-VAE to grow with the complexity of the data in comparison to the c-VAE and discriminative CNN model.

Confounder disentanglement: Because confounder factors are unobserved in the clinical dataset, we use the anonymized patient ID as a *weak* label of the confounders. We then test, for cIBP-VAE, to which extent we can use each of the learned latent representations (y_t and y_c) to classify the task label (pacing segments) and confounder label (patient ID). This is done by training separate support vector machines (SVMs) with a linear kernel to associate each of the latent representation to each label. The results are summarized in Table 2 in the dataset with and without the pacing artifacts. Note that, because we have distinct patients on the training, validation and test set, the classification accuracy involving confounding factor y_c is reported on the training dataset. First, as shown, y_t and y_c are each more informative about their respective labels than the other, demonstrating successful disentanglement. Second, the introduction of an additional confounding factor has a minimal effect on the ability of the presented cIBP-VAE to disentangle.

model	all signal	only artifacts		
		all	non-stimulus	stimulus
c-VAE	2293.23	3.20	3.91	2.49
cIBP-VAE	2273.65	0.45	0.19	0.72

Table 3: Quantitative reconstruction errors in c-VAE versus cIBP-VAE. Column 2 (all signal): reconstruction errors for the entire signal including artifacts. Columns 3-5 (only artifacts): reconstruction errors for the artifact portion of the signal, including that calculated for all samples (*all*), samples with no pacing artifact (*non-stimulus*), and samples with pacing artifacts (*stimulus*).

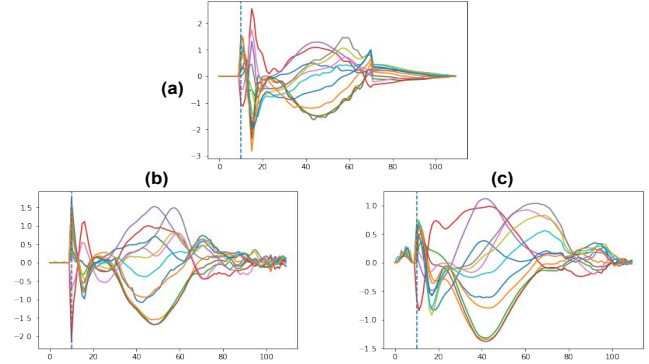


Figure 3: 12-lead ECG traces where the pacing artifact is highlighted to the left side of the dotted line. (a) The original signal without the pacing artifact, (b) reconstructed signal using the presented cIBP-VAE and (c) reconstructed signal using c-VAE.

Uncovering latent factors: We then focus on the ability of the two VAE generative models in uncovering the binary factor of pacing artifacts in the augmented dataset.

Reconstruction accuracy: In terms of reconstruction error, we note that while cIBP-VAE and c-VAE show a similar overall performance (Table 3, first column), the results may be deceiving because the pacing artifact constitutes only a small component of the overall quantitative reconstruction error. If we focus on only the portion of the pacing artifacts, c-VAE demonstrates a higher error in reconstructing data without pacing-artifacts (Table 3, second column). An example is shown in 3, where cIBP-VAE was able to reconstruct the absence of a pacing artifact while c-VAE was not. More examples are provided in the supplementary material (3.1). The reported results are found to be statistically significant (p-value < 0.01). This ability to qualitatively identify the absence or presence of a binary confounding factor is an important advantage of the presented cIBP-VAE model.

Identification of the binary factor: To understand the ability of the cIBP-VAE to capture the binary confounding factor of pacing artifacts, we further analyzed the latent binary features in the cIBP-VAE model. Throughout all test cases, we find that ECG data with the pacing artifact is encoded into 24 active binary features, while data without the pacing artifact are encoded into 25 active binary features. In another word, the activation or deactivation of one dimen-

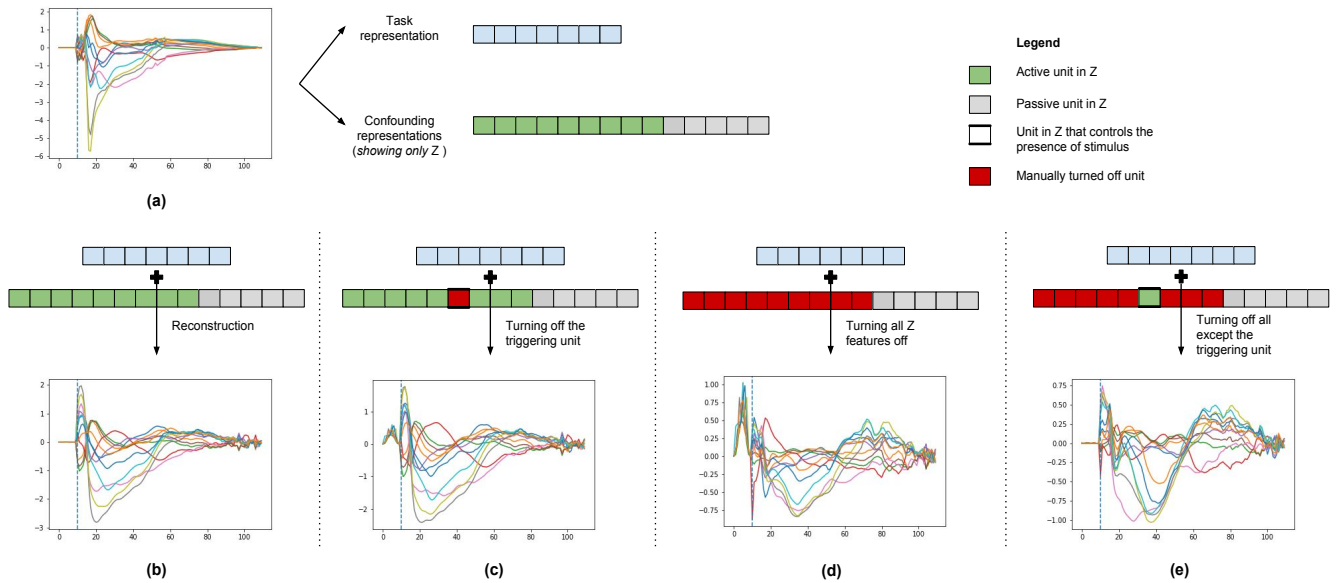


Figure 4: [Best viewed in color] (a) Original signal without artificial pacing stimulus decomposed into task-based representation and confounding representation (schematically shown), (b) regular reconstruction, (c) signal generated by turning-off only the triggering unit, (d) signal generated by turning off all the active units of Z , and (e) signal generated by turning off all the active units except the triggering unit.

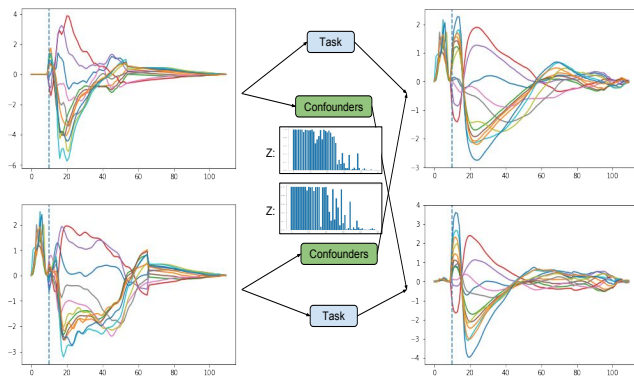


Figure 5: Swapping between the task-relevant representations and confounding representation from two samples (left) generate two new signals with swapped presence and absence of pacing artifact (right). The plots of Z show the number of active features for the confounding representations for each signal, where the number is higher for the signal without the artifact.

sion in the latent binary representations Z is identifying the absence or presence of the confounding artifact in the given data. Through extensive testing of the trained cIBP-VAE, we were able to identify this specific *triggering unit*.

An example of an ECG signal without pacing artifact is illustrated in Figure 4. Comparing 4(b) and 4(c), it is evident that the de-activation of the triggering unit activates a pacing artifact in the reconstructed signal (4(c)). A further examination by turning off all the confounding features in Figure 4 (d) revealed that the model has learned to encode the infor-

mation about the pacing artifact into the task-relevant representation. Only by activating the triggering unit, as shown in Figure 4 (e), the pacing artifact is de-activated. This shows that, in this dataset, the cIBP-VAE has learned to encode the absence of a signal artifact as a binary latent factor which, when activated, denotes the absence of the artifact.

In Figure 5, we further demonstrate that by swapping the encoded confounding representation between a pair of signals with and without pacing artifact, the absence, and presence of the pacing artifacts are transferred as well.

Conclusion and Future Work

The paper presents a deep conditional generative model and the associated approximative inference scheme for disentangling and learning the unobserved and unbounded number of confounding factors present in the data. On colored MNIST and clinical ECG dataset in comparison with the standard conditional VAE and other conventional approaches, the presented model demonstrated an increased efficacy in learning the task-relevant representations. More importantly, the presented model reveal the ability to identify and control the absence or presence of binary confounding factors. Future work will focus on improving the presented model with convolutional or recurrent modules in the encoder and decoder, and test it in a larger variety of applications where the confounding factors are known to be unbounded. It will also be interesting to further analyze the performance of the model in more controlled settings where the label information for all or most of the confounding factors is known and can be used for evaluation.

References

- [Bengio, Courville, and Vincent 2013] Bengio, Y.; Courville, A.; and Vincent, P. 2013. Representation learning: A review and new perspectives. *IEEE transactions on pattern analysis and machine intelligence* 35(8):1798–1828.
- [Burda, Grosse, and Salakhutdinov 2015] Burda, Y.; Grosse, R.; and Salakhutdinov, R. 2015. Importance weighted autoencoders. *arXiv preprint arXiv:1509.00519*.
- [Chatzis 2014] Chatzis, S. P. 2014. Indian buffet process deep generative models. *arXiv preprint arXiv:1402.3427*.
- [Chen et al. 2016a] Chen, X.; Duan, Y.; Houthoofd, R.; Schulman, J.; Sutskever, I.; and Abbeel, P. 2016a. Infogan: Interpretable representation learning by information maximizing generative adversarial nets. In *Advances in Neural Information Processing Systems*, 2172–2180.
- [Chen et al. 2016b] Chen, X.; Kingma, D. P.; Salimans, T.; Duan, Y.; Dhariwal, P.; Schulman, J.; Sutskever, I.; and Abbeel, P. 2016b. Variational lossy autoencoder. *arXiv preprint arXiv:1611.02731*.
- [Chen et al. 2017] Chen, S.; Gyawali, P. K.; Liu, H.; Horacek, B. M.; Sapp, J. L.; and Wang, L. 2017. Disentangling inter-subject variations: Automatic localization of ventricular tachycardia origin from 12-lead electrocardiograms. In *Biomedical Imaging (ISBI 2017), 2017 IEEE 14th International Symposium on*, 616–619. IEEE.
- [Dilokthanakul et al. 2016] Dilokthanakul, N.; Mediano, P. A.; Garnelo, M.; Lee, M. C.; Salimbeni, H.; Arulkumaran, K.; and Shanahan, M. 2016. Deep unsupervised clustering with gaussian mixture variational autoencoders. *arXiv preprint arXiv:1611.02648*.
- [Goyal et al. 2017] Goyal, P.; Hu, Z.; Liang, X.; Wang, C.; Xing, E. P.; and Mellon, C. 2017. Nonparametric variational auto-encoders for hierarchical representation learning. In *ICCV*, 5104–5112.
- [Griffiths and Ghahramani 2011] Griffiths, T. L., and Ghahramani, Z. 2011. The indian buffet process: An introduction and review. *Journal of Machine Learning Research* 12(Apr):1185–1224.
- [Higgins et al. 2016] Higgins, I.; Matthey, L.; Pal, A.; Burgess, C.; Glorot, X.; Botvinick, M.; Mohamed, S.; and Lerchner, A. 2016. beta-vaе: Learning basic visual concepts with a constrained variational framework.
- [Hoffman and Blei 2015] Hoffman, M. D., and Blei, D. M. 2015. Structured stochastic variational inference. In *Artificial Intelligence and Statistics*.
- [Ioffe and Szegedy 2015] Ioffe, S., and Szegedy, C. 2015. Batch normalization: Accelerating deep network training by reducing internal covariate shift. In *International Conference on Machine Learning*, 448–456.
- [Kingma and Ba 2014] Kingma, D., and Ba, J. 2014. Adam: A method for stochastic optimization. *arXiv preprint arXiv:1412.6980*.
- [Kingma and Welling 2013] Kingma, D. P., and Welling, M. 2013. Auto-encoding variational bayes. In *Proceedings of the 2nd International Conference on Learning Representations (ICLR)*, number 2014.
- [Kingma et al. 2014] Kingma, D. P.; Mohamed, S.; Rezende, D. J.; and Welling, M. 2014. Semi-supervised learning with deep generative models. In *Advances in Neural Information Processing Systems*, 3581–3589.
- [Kulkarni et al. 2015] Kulkarni, T. D.; Whitney, W. F.; Kohli, P.; and Tenenbaum, J. 2015. Deep convolutional inverse graphics network. In *Advances in Neural Information Processing Systems*, 2539–2547.
- [LeCun et al. 1998] LeCun, Y.; Bottou, L.; Bengio, Y.; and Haffner, P. 1998. Gradient-based learning applied to document recognition. *Proceedings of the IEEE* 86(11):2278–2324.
- [Louizos et al. 2015] Louizos, C.; Swersky, K.; Li, Y.; Welling, M.; and Zemel, R. 2015. The variational fair autoencoder. *arXiv preprint arXiv:1511.00830*.
- [Maddison, Mnih, and Teh 2016] Maddison, C. J.; Mnih, A.; and Teh, Y. W. 2016. The concrete distribution: A continuous relaxation of discrete random variables. *arXiv preprint arXiv:1611.00712*.
- [Nalisnick and Smyth 2016] Nalisnick, E., and Smyth, P. 2016. Stick-breaking variational autoencoders. *arXiv preprint arXiv:1605.06197*.
- [Paszke et al. 2017] Paszke, A.; Gross, S.; Chintala, S.; Chanan, G.; Yang, E.; DeVito, Z.; Lin, Z.; Desmaison, A.; Antiga, L.; and Lerer, A. 2017. Automatic differentiation in pytorch. In *NIPS-W*.
- [Rezende, Mohamed, and Wierstra 2014] Rezende, D. J.; Mohamed, S.; and Wierstra, D. 2014. Stochastic back-propagation and approximate inference in deep generative models. In *Proceedings of the 31th International Conference on Machine Learning, ICML 2014, Beijing, China, 21-26 June 2014*, 1278–1286.
- [Sapp et al. 2012] Sapp, J. L.; El-Damaty, A.; MacInnis, P. J.; Warren, J. W.; and Horáček, B. M. 2012. Automated localization of pacing sites in postinfarction patients from the 12-lead electrocardiogram and body-surface potential maps. *Computing in Cardiology*.
- [Singh, Ling, and Doshi-Velez 2017] Singh, R.; Ling, J.; and Doshi-Velez, F. 2017. Structured variational autoencoders for the beta-bernoulli process. *NIPS 2017 Workshop on Advances in Approximate Bayesian Inference*.
- [Skelly, Dettori, and Brodt 2012] Skelly, A. C.; Dettori, J. R.; and Brodt, E. D. 2012. Assessing bias: the importance of considering confounding. *Evidence-based spine-care journal* 3(01):9–12.
- [Stevenson 2009] Stevenson, W. G. 2009. Ventricular scars and ventricular tachycardia. *Transactions of the American Clinical and Climatological Association* 120:403.
- [Teh, Grür, and Ghahramani 2007] Teh, Y. W.; Grür, D.; and Ghahramani, Z. 2007. Stick-breaking construction for the indian buffet process. In *Artificial Intelligence and Statistics*, 556–563.
- [Thibaux and Jordan 2007] Thibaux, R., and Jordan, M. I.

2007. Hierarchical beta processes and the indian buffet process. In *Artificial Intelligence and Statistics*, 564–571.

[Wang and Deng 2018] Wang, M., and Deng, W. 2018. Deep visual domain adaptation: A survey. *Neurocomputing*.

[Wu et al. 2018] Wu, Z.; Wang, H.; Cao, M.; Chen, Y.; and Xing, E. P. 2018. Fair deep learning prediction for healthcare applications with confounder filtering. *arXiv preprint arXiv:1803.07276*.

[Yokokawa et al. 2012] Yokokawa, M.; Liu, T.-Y.; Yoshida, K.; Scott, C.; Hero, A.; Good, E.; Morady, F.; and Bogun, F. 2012. Automated analysis of the 12-lead electrocardiogram to identify the exit site of postinfarction ventricular tachycardia. *Heart Rhythm* 9(3):330–334.

[Zemel et al. 2013] Zemel, R.; Wu, Y.; Swersky, K.; Pitassi, T.; and Dwork, C. 2013. Learning fair representations. In *International Conference on Machine Learning*, 325–333.

Supplementary material

Implementation details

Concrete distribution During training of our presented cIBP-VAE, we approximate Bernoulli random variables Z with the *Concrete distribution* (Maddison, Mnih, and Teh 2016) which has a convenient parametrization:

$$\tilde{z} = \text{sigmoid}\left(\frac{1}{\tau} (\log(\pi_k) + g)\right) \quad (7)$$

where τ is the temperature parameter, g is the sample from the Gumbel(0,1) distribution which again has a convenient sampling strategy using Uniform(0,1).

Kumaraswamy distribution For the posterior involving Beta distribution, we approximate using the Kumaraswamy distribution as shown by (Nalisnick and Smyth 2016) where samples are drawn as:

$$\nu \sim \text{Uniform}(0,1)^{\frac{1}{a}} \text{Uniform}(0,1)^{\frac{1}{b}} \quad (8)$$

where $u \sim \text{Uniform}(0,1)$ and $a, b > 0$. This distribution is equivalent to Beta distribution when $a = 1$ or $b = 1$ or both.

KL between Kumaraswamy-Beta As shown in (Nalisnick and Smyth 2016), the Kullback-Leibler divergence between the $q(\nu_k) \sim \text{Kumaraswamy}(a, b)$ and $p(\nu_k) \sim \text{Beta}(\alpha, \beta)$ distribution is

$$KL(q(\nu_k) \parallel p(\nu_k)) = \frac{a}{\alpha} \left(\gamma - \Psi\left(\frac{a}{b}\right) \right) + \log ab + \log B(\alpha, \beta) - \frac{b}{\beta} \frac{1}{b} + (\beta - 1)b \sum_{m=1}^{\infty} \frac{1}{m + ab} B\left(\frac{m}{a}, b\right) \quad (9)$$

where γ is Euler’s constant, $\Psi(\cdot)$ is the Digamma function, and $B(\cdot)$ is the Beta function. In practice, a finite approximation of the infinite sum is used.

Experiments

QRS Integral A linear model using commonly-used prescribed features of 120-ms QRS-integrals is considered for

localizing the ventricular activation previously in the literature (Sapp et al. 2012). The standard trapezoidal rule (Matlab function *trapz*) is used to extract the integral features from the QRS complex of each lead of ECG. The extracted integral features from all the 12 leads are concatenated together. Because of the differences in the study population, the direct comparison with the reported results in the literature is difficult and thus, we compared the proposed approach with QRS Integral.

A hidden linear layer with 10 units is used to transform input features of size 12 (12 leads). The *softmax* function is used to convert them to one hot vector. The SGD optimizer with the learning rate of 0.002 is used to train the model.

CNN Three layered convolution block followed by two fully connected layers are considered in this setup. The architecture includes dropout and rectified linear units (ReLU) as an activation function. The input data is re-arranged as 12x100 because of spatial convolution used in this setting. Further, we also incorporated recently introduced batch normalization (Ioffe and Szegedy 2015) which enables faster and more stable training of the network by stabilizing the distribution of layers input which is achieved by reducing internal covariate shift of mini-batches. The architecture is trained with SGD using learning rate = 0.0001, momentum = 0.9 and weight decay = 0.0001. The detail architecture is presented below in Table 2.

Layer	Info
CNN ₁	2dConv(1, 32, (3,5), 1), batchNorm, ReLU, 2dMaxPool(1, 2, stride=(2,2))
CNN ₂	dropout (0.5), 2dConv(32, 24, (3,3), 1), batchNorm, ReLU, 2dMaxPool(1, 2, stride=(1,1))
CNN ₃	dropout (0.5), 2dConv(24, 12, (1,1), stride=1), batchNorm, ReLU, 2dMaxPool(1, 1, stride=(1,1))
FC ₁	dropout (0.5), Linear layer(200), batchNorm, ReLU
FC ₂	dropout (0.5), Linear layer(10), Softmax

Table 4: The detailed architecture of CNN used in the paper.

Results

Clinical ECG dataset In Figure 6, we present four examples of reconstruction of clinical ECG samples (augmented with the artifacts) for cIBP-VAE compared against c-VAE.

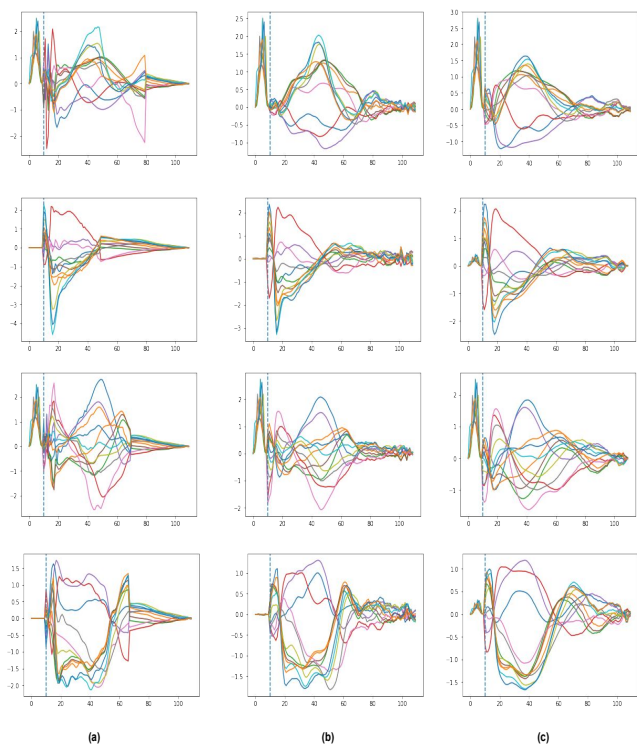


Figure 6: Reconstruction comparison between cIBP-VAE and c-VAE. **(a)**original signals **(b)** reconstructions from cIBP-VAE and **(c)** reconstructions from c-VAE.